Modeling Plasma Processes in 1-Kilowatt Hydrazine Arcjet Thrusters

Thomas W. Megli,* Junqing Lu,† Herman Krier,‡ and Rodney L. Burton§
University of Illinois at Urbana–Champaign, Urbana, Illinois 61801

This paper presents predictions of a nonequilibrium 1-kW hydrazine arcjet model with sensitivity studies on generalized Ohm's law and electron–molecule inelastic collision factor δ. This model treats steady-state, two-dimensional, axisymmetric, two-temperature (electrons and heavy species), chemical nonequilibrium viscous flow, and includes flow swirl and anode heat transfer in a converging–diverging nozzle. Key results indicate that the arcjet flow is in thermal and chemical nonequilibrium. Sensitivity studies show that the modeling of the inelastic coupling of electrons–molecules significantly alters the predicted anode current attachment location and, subsequently, the predicted plasma voltage drop, and that the electron pressure gradient term does not significantly affect the current distribution. With an appropriate choice of δ, and adopting values from the literature for the cathode and anode sheath voltages, the model predictions are in good agreement with the experimental values.

Nomenclature

B = magnetic field, T
C_{pe} = thermodynamic function for electrons, J
E = electric field, V/m
e = electric charge, C
$elst$ = elastic energy transfer, W/m^3
f = mass fraction of unionized atoms; or electron energy distribution function, eV$^{-3/2}$
g_0 = gravitational acceleration at sea level, m/s^2
I = current, A
I_{sp} = specific impulse, s
j = current density, A/m^2
k_b = Boltzmann's constant, J/K
L_e = individual energy loss rate, J/s
$\dot{m}$ = mass flow rate, mg/s
m_i = mass of species i, kg
N = total particle number density, m^{-3}
n_e = electron number density, m^{-3}
n_i = number density of heavy species i, m^{-3}
P = electric power, W
p = pressure, N/m^2
p_e = electron pressure, N/m^2
Q_{ei} = collision cross section between electrons and heavy species i, m^2
T_a = anode temperature, K
T_e = electron temperature, K
T_g = heavy-species temperature, K
u = axial velocity, m/s
V = voltage, V
v = radial velocity, m/s
v = velocity vector, m/s
w = azimuthal swirl velocity, m/s

x_{cat} = cathode gap, mm
x_i = mole fraction of species i
x, r, θ = cylindrical conditions
y_e = mass fraction of electrons
α = nozzle half-angle, or degree of ionization
δ_i = electron–molecule inelastic loss factor for species i
ε = electron energy, eV
η = thrust efficiency
λ_e = electron thermal conductivity, W/m-K
$\bar{v}_{ei}$ = average collision frequencies between electrons and heavy species i, s^{-1}
ρ = mass density, kg/m^3
σ = electric conductivity, $(\Omega\text{-m})^{-1}$
τ_{In} = collision time for ions and neutrals, s

Introduction

A CHALLENGING and important area of satellite propulsion is the application of low-power thrusters, and, in particular, the arcjet thruster. Typically, a specific impulse significantly higher than 400 s is called for to provide greatly increased payload mass fraction for high ΔV missions such as low Earth orbit–geosynchronous (LEO–GEO) orbit transfer. Further development requires an understanding of the internal energy transfer and flow processes in 1-kW class hydrazine arcjets, and, in particular, modeling of the thermal and chemical nonequilibrium in the flow. This paper continues the development of the 1-kW hydrazine arcjet model developed by Megli, Krier, and Burton (the MKB model).[1]

It has been determined empirically that, for arcjets in the 1-kW range, the most important issues are constrictor and anode life, which are mostly affected by heating in the constrictor region. An understanding of current attachment and anode heating is required, and can be achieved with a validated plasmadynamics model. In addition to the MKB model, two existing hydrogen arcjet models[2,3] are capable of modeling two-dimensional thermal and chemical nonequilibrium arcjet physics. The emphasis here has been on development of a thermophysical flow modeling tool, coupled with detailed experimental boundary measurements of plasma parameters, with model validation as the primary goal. This approach is expected to produce a relatively complete understanding of the plasmadynamics of 1-kW arcjets and to predict arcjet performance at high $P/\dot{m}$.

Description of the Arcjet Thruster

The azimuthally symmetric arcjet is shown schematically in Fig. 1. The fluid dynamics and energy transfer within the

*Ph.D. Candidate, Department of Mechanical and Industrial Engineering, 1206 West Green Street; currently Engineering Specialist, Ford Research and Engineering Center, 21500 Oakwood Boulevard, Dearborn, MI 48121. Member AIAA.
†Graduate Student, Department of Mechanical and Industrial Engineering, 1206 West Green Street. Member AIAA.
‡Professor, Department of Mechanical and Industrial Engineering, 1206 West Green Street. Fellow AIAA.
§Professor, Department of Aeronautical and Astronautical Engineering, 104 South Wright Street. Associate Fellow AIAA.
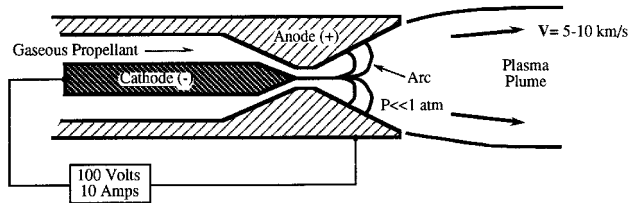
Fig. 1 Schematic of a typical electrothermal arcjet thruster. A voltage difference between the cathode and anode produces an electric discharge, which heats the propellant. The thermal energy is converted to kinetic energy as the propellant expands to high velocities in the converging–diverging nozzle.

thruster are nonlinear and strongly coupled. The propellant is injected upstream of the constrictor, typically with an azimuthal (or swirl) velocity component. The energy conversion mechanism for an arcjet is an arc discharge, produced by a voltage difference between the thruster nozzle, which is the anode, and a conical cathode on the upstream side of the constrictor. Electron current is supplied by field-enhanced thermionic emission from the cathode tip. Typical operating voltages for 1-kW class arcjets are about 115 V dc, with $I = 10$ A. The arc current distribution depends on several factors in addition to the geometry, and is coupled to the propellant mass flow rate, composition, thermal properties, electric conductivity, and gasdynamic properties.

Both chemical and thermal processes in the arcjet are in nonequilibrium. Arc current is converted to electron thermal energy through ohmic dissipation. The electrons transfer thermal energy to the heavy species in the arc plasma through collisions. This thermal energy is then converted to kinetic energy and, therefore, thrust as the fluid accelerates through the nozzle. In regions of low pressure and/or elevated ohmic heating, collisional coupling between electrons and heavy species may not establish equal gas and electron temperatures. Additionally, flow velocities are large, so that fluid residence time in the nozzle is on the order of 1 μs. Thus, much of the energy invested in dissociation and ionization is frozen. The pressure drops from roughly 1 atm at the constrictor to torr conditions at the exit. The radial diffusion of electrons from the arc core is important in determining the arc structure.

Small mass flow rates of tens of milligrams per second are used to operate the thruster at a $P/\dot{m}$ of 15–45 MJ/kg. Typical 1-kW-class arcjet thrusters have constrictor diameters of 0.6 mm, with nozzle expansion half-angles of 20 deg and exit diameters of 9 mm. Velocities vary from approximately 10 km/s on the centerline to 0 at the wall, with gas temperatures ranging from 20,000 K near the cathode tip to roughly 1500 K at the anode.[1] Despite the high velocities, the arcjet is a viscous, low-Reynolds number device [$Re = \mathbb{O}(100-1000)$] because of low mass flow rates, high gas temperatures, and millimeter-size dimensions.

The thrust and specific impulse produced by an arcjet are determined by several factors, including 1) the power transferred to the propellant, 2) the extent of both thermal and chemical nonequilibrium, 3) the propellant gas mixture, 4) viscous losses, and 5) arcjet nozzle geometry. Factors that detract from performance include heat loss to the anode and the voltage sheaths at the electrodes. A comprehensive model of an arcjet thruster is highly complex, and must include plasmadynamic, fluid-dynamic, and surface and volumetric heat transfer phenomena.[1,4]

The energy loss mechanisms can be more readily appreciated by examining the η of the device, which is a measure of the ratio of the directed kinetic power of the exiting propellant to the electric power input:

$$\eta = \frac{\dot{m}u^2}{2P} = \frac{\dot{m}I_{sp}^2 g_0^2}{2P} \qquad (1)$$

The thrust efficiencies of 35%, typical of 1-kW arcjets, clearly indicate significant room for design improvements through the reduction of frozen flow and viscous, electric sheath, and heat transfer losses.

MKB Arcjet Model

The MKB arcjet model is a steady, two-dimensional, axisymmetric, two-temperature, chemical nonequilibrium model that includes flow swirl and anode heat transfer in a converging–diverging nozzle geometry with variable cathode gap. The model assumes the radiating plasma to be optically thin.[1] The gas is simulated hydrazine, $0.5N_2 + H_2$. Input parameters are thruster geometry, mass flow rate, total applied current, and inlet flow swirl velocity.

The model predicts thrust, specific impulse, and internal fields for p, ρ, and seven n_i, as well as T_a, T_e, and T_g. Additionally, the model predicts the j distribution, V potential, and u, v, and w.

Equations in Refs. 1 and 4 model 1) fluid dynamics, 2) electron and heavy-species energy, 3) electromagnetics, 4) species number densities, 5) transport coefficients, and 6) boundary conditions. The arcjet geometry is described as (x, r, θ), representing the axial, radial, and azimuthal coordinates, respectively.

The important assumptions are 1) axisymmetric, steady, continuum, and viscous nozzle flow; 2) Maxwellian energy distributions for electrons and heavy species; 3) independent relations for electron energy (temperature) and heavy-species energy (temperature) for atoms, molecules, and ions, coupled by elastic and inelastic collisions and radiation; 4) for N_2H_4 (hydrazine) arc-heating, finite rate chemistry for dissociation, ionization, and their reverse reactions (considers 11 reactions); 5) generalized Ohm's law for current density; 6) two-dimensional heat conduction in anode; 7) multicomponent, energy-averaged collision integrals for calculations of the mixture transport properties (viscosity, diffusivity, and conductivity); 8) neutral plasma, i.e., $n_e = n_{H^+} + n_{N^+}$; 9) ideal (mixture) two-temperature plasma equation of state: $p = n_e k_b T_e + (n_{N_2} + n_{H_2} + n_N + n_H + n_e) k_b T_g$; 10) individual species conservation and diffusion (affects energy conservation as chemical source terms); 11) total pressure (≈ 3 atm) fixes mass flow at inlet; 12) at supersonic nozzle exit plane, static pressure is extrapolated from flow interior, despite presence of a mixed supersonic and (annular) subsonic flow; 13) anode is modeled as an equipotential ($V = 0$) surface; 14) cathode sheath voltage of 30 V (from cathode sheath models[5]) and anode sheath voltage of 11 V (from anode probe measurements[6]) are added to the plasma voltage to yield total arcjet voltage; and 15) geometry is modeled as the NASA 1-kW arcjet.[7]

The computational grids are composed of 62 axial by 17 radial nodes for the plasma, and 62 axial by 9 radial nodes for the anode domain.[1] The grids are tuned such that denser grids are located near the electrode surfaces and the constrictor, where gradients in plasma properties are large.[1] A recent grid study demonstrated that this grid system cannot be refined without violating the continuum assumption of the model.[5]

Baseline Flowfield Results for Hydrazine

The characteristics of the plasma flowfield were investigated for the NASA Lewis Research Center's 1-kW thruster.[1,4,8] In Ref. 8, chemical equilibrium (CE) and chemical nonequilibrium (CNE) predictions are compared for the velocity, temperature, current density, and number densities. These results correspond to cases 1 and 2 shown in Table 1.

The CE and CNE hydrazine simulations are systematically compared in Figs. 2 and 3, demonstrating the necessity of CNE formulation. At the cathode tip, the current density is 40,000 A/cm^2 for the CE case. A peak anode attachment current density of 18 A/cm^2 is noted at a location of $x \approx 11$ mm, or roughly 5 mm downstream of the constrictor. The anode temperature increases from the upstream boundary value of 1000

Table 1 Summary of predictions for 1-kW hydrazine (N_2H_4) arcjets operating at 10 A and approximately 50 mg/s[a]

Case	∇p_e term	δ_N	δ_H	x_{cat}, mm[b]	Total voltage, V[c]	I_{sp}, s	η, %
1[d]	N	3000	3000	0.58	141	440	33
2	N	3000	3000	0.58	115	439	40
3	N	3000	3000	1.02	122	446	39
4	N	300	300	1.02	115	440	40
5	N	30	30	1.02	104	423	41
6	Y	Variable	Variable	0.58	88	402	44
7	Y	3000	10	0.58	99	414	42
8	Y	4000	10	0.58	101	416	41
9	Y	3000	3000	0.58	112	436	41
10 (experimental)[e]	——	——	——	0.58	115	419	35

[a]Geometry is the NASA Lewis Research Center Arcjet.[7]
[b]Cathode gap spacing, measured axially from the cathode surface to the converging portion of the anode surface.
[c]Total voltage predictions include a cathode sheath voltage of 30 V (Ref. 5) and an anode sheath voltage of 11 V (Ref. 6).
[d]This is the only CE case.
[e]Experimental values are from Ref. 7.
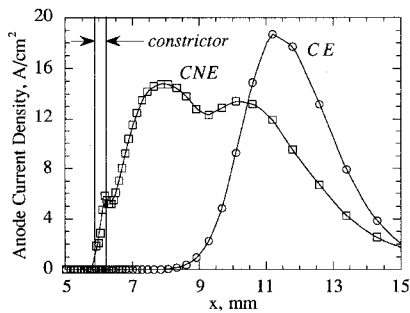
Fig. 2 Current density at the anode surface for simulated hydrazine. Results are shown for both CE and CNE simulations (predictions for cases 1 and 2 of Table 1).
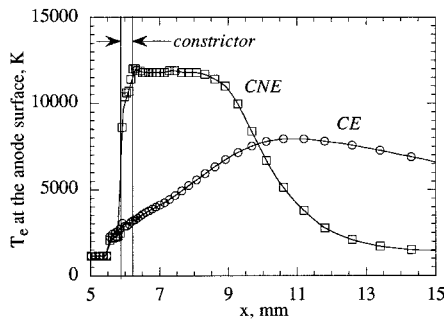
Fig. 3 Electron temperature at the anode surface for simulated hydrazine. Results are shown for both CE and CNE simulations (predictions for cases 1 and 2 of Table 1).

K to about 1300 K near the exit plane. For the CNE hydrazine simulation, the peak anode that is $j \approx 15$ A/cm^2 occurs when $x \approx 8$ mm, upstream from that for the CE case. The CNE anode temperature is somewhat lower than for CE, with a value of about 1200 K at the exit plane.

The marked difference in the current attachment predictions is clearly illustrated in Fig. 2, where the anode current densities are indicated. For CNE, a more diffuse, bimodal distribution is noted, with the attachment closer to the constrictor. The voltage prediction for CNE (115 V) is 23% lower than that for CE (141 V) (Table 1), casting doubt about the CE assumption.

The anode/plasma interface T_e distributions are indicated in Fig. 3. A high degree of thermal nonequilibrium is noted, with maximum electron temperatures of approximately 8000 and 12,000 K for the CE and CNE simulations, respectively. The thermal nonequilibrium condition largely controls the near-anode electron densities, which in turn determine the electric conductivity of the plasma. For the CNE simulations, increased ionization rate coefficients are predicted by the elevated T_e. The mechanism of arc attachment captured by this model is the increased ionization fractions predicted by the relatively high near-anode T_e, although these fractions are only $\mathbb{O}(10^{-4})$. Radial diffusion of electrons from the arc core also enhances the electron populations. These processes give a finite, nonzero prediction for the electric conductivity near the electrodes where T_g is low.

Although both CE and CNE results indicate significant thermal nonequilibrium near the anode, the central region of the arc is near equilibrium.[1,4,8] For example, a maximum $T_g \approx$ 22,000 K occurs near the center of the constrictor for CE hydrazine, and a maximum $T_e \approx$ 25,000 K occurs at the same location.[4,8] The higher ionization fractions on centerline efficiently couple the electron and gas temperatures through coulombic collisions between the electrons and ions. The results for CNE hydrazine are similar, with maxima of $T_g \approx$ 22,000 K and $T_e \approx$ 28,000 K.[1,8]

Arcjet conditions can indicate when finite rate chemistry must be included to predict frozen flow losses accurately. Bose warned that the results from the Saha Equation[9] would be incorrect if the electron temperature is more than twice the heavy-species temperature. Richley and Tuma[10] further recommended that the difference between the electron temperature and the heavy-species temperature should not exceed 2000 K, otherwise, finite rate chemistry should replace the Saha equation. CNE conditions therefore exist here.

In Figs. 4 and 5, exit plane predictions of n_e are presented. The Saha-predicted centerline n_e for CE (Fig. 4) hydrazine = 1.6×10^{11} cm^{-3}, whereas the n_e for CNE (Fig. 5) is 3 orders of magnitude higher: 1.6×10^{14} cm^{-3}. The CNE predictions for centerline distributions of electron density are in better agreement with the internal nozzle measurements of Zube and Myers.[1,4,11]

Also shown in Figs. 4 and 5 are T_e and T_g profiles. More thermal nonequilibrium is indicated for the CE case with $T_e/T_g \approx 2.0$ at the centerline, whereas the CNE case is near equilibrium at $T_e/T_g \approx 1.1$. The degree of thermal nonequilibrium scales inversely with electron density, so that the lower electron concentrations predicted for CE translate directly to higher predicted exit plane electron temperatures.

The reason for CNE is twofold. First, competing rate processes have different temperature dependencies, which are not captured by the CE formulation. Second, the arcjet flow has high velocity and low residence time inside the nozzle, thus, the reactions do not have enough time to reach the equilibrium
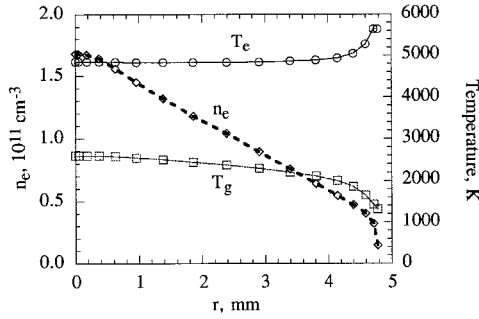
Fig. 4   Radial distributions of electron number density, electron temperature, and heavy-species temperature at the exit plane for the hydrazine CE case 1 of Table 1.
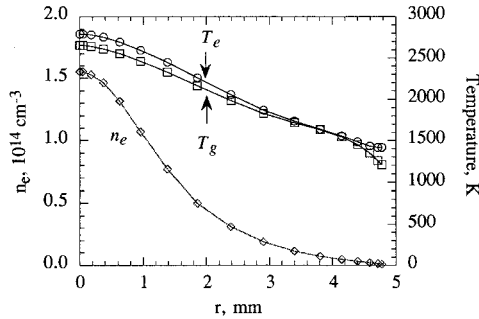

Fig. 5   Radial distributions of electron number density, electron temperature, and heavy-species temperature at the exit plane for the hydrazine CNE case 2 of Table 1.
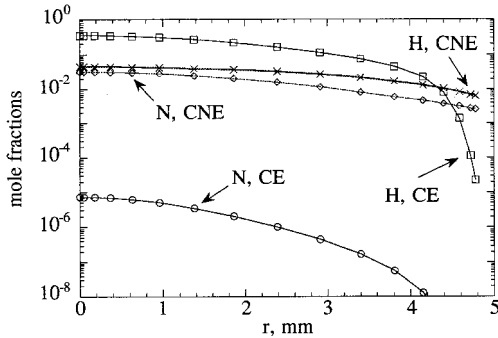

Fig. 6   Radial distributions of H- and N-atom mole fractions at the exit plane for the hydrazine CE and CNE simulations (predictions for cases 1 and 2 of Table 1).

state. The MKB model results indicate that the electron temperature is an order of magnitude higher than the heavy-species temperature near the anode and the fluid residence time in the nozzle is on the order of 1 μs, so that finite rate chemistry, i.e., CNE, should be used.

The results for H- and N-atom mole fractions at the arcjet exit plane are shown in Fig. 6. The CNE radial profiles are generally smoother in the central portion of the flow because of radial diffusion. The CE predictions for N-atom mole fractions are several orders of magnitude lower than those for CNE, with centerline values of 1×10^{-5} and 3×10^{-2}, respectively. This is in contrast to the centerline predictions for H-atom mole fractions, where CE calculations indicate a significantly higher H dissociation fraction in the center of the flow. The respective centerline mole fractions for H in CE and CNE are 0.35 and 0.04.

Results for H_2 and N_2 mole fractions are shown in Fig. 7. Again, the effects of radial diffusion are evident, with smoother profiles indicated for the CNE predictions, and elevated molecular mole fractions in the hotter central region of the flow. At the anode wall ($r \approx 4.8$ mm), both the CNE and

CE mole fraction predictions are approximately that of the inflowing propellant ($N_2 + 2H_2$ for simulated hydrazine), with $x_{H_2} \approx 0.67$ and $x_{N_2} \approx 0.33$. Centerline H_2 mole fractions of 0.58 and 0.38 are indicated for the CNE and CE simulations, respectively. The diffusive effects are less pronounced for the heavier N_2 molecule. Centerline values for the respective CNE and CE simulations are $x_{N_2} \approx 0.30$ and 0.28, respectively.

Voltage contours are shown in Fig. 8 (note that the sheath voltage contributions have not been added to the contours shown here). Even outside the sheath, strong electric fields are noted near the electrode surfaces. At the cathode tip, the plasma voltage decreases axially from 74 to 67 V (only the magnitude of the voltages is listed, following the convention for arcjet literature) over a distance of $\Delta x \approx 0.03$ mm, indicating a strong E of ≈ 230 V/mm. The net axial voltage rise across the constrictor is roughly $\Delta V \approx 34$ V, corresponding to an average E of ≈ 136 V/mm. The plasma voltage drop predicted from current conservation and Ohm's law is 74 V. The total arcjet voltage is 115 V, including 30 V from the cathode sheath[5] and 11 V from the anode sheath.[6] This indicates that 56% of the arcjet power is deposited in the constrictor. Strong radial gradients in voltage are also noted near the anode. A 13-V drop at an axial location of $x \approx 7$ mm occurs over a radial distance of $\Delta r \approx 0.05$ mm. This gives an estimate for $E \approx 260$ V/mm.

Ohmic heating contours proportional to j^2/σ are plotted in Fig. 9. In the constrictor, the small cross-sectional area and the strong axial electric fields produce high current density and
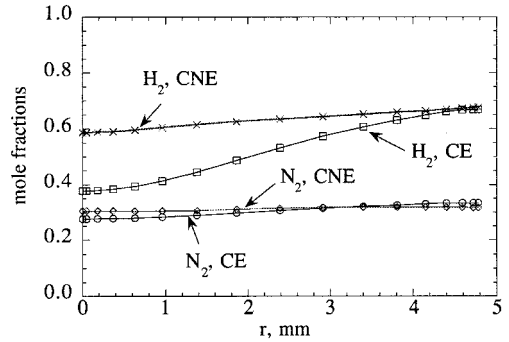

Fig. 7   Radial distributions of H_2- and N_2-molecule mole fractions at the exit plane for the hydrazine CE and CNE simulations (predictions for cases 1 and 2 of Table 1).
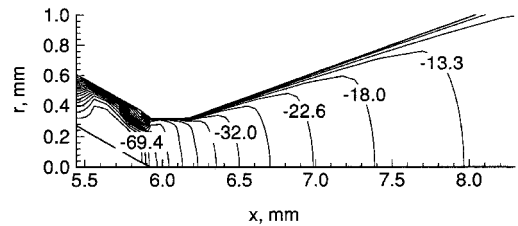

Fig. 8   Voltage contours, V, for the NASA Lewis Research Center's arcjet; simulated hydrazine, CNE simulation, $I = 10$ A, $\dot{m} \approx 50$ mg/s (case 2 of Table 1).

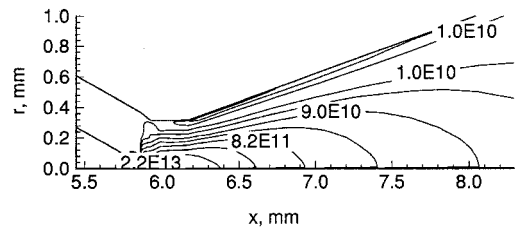**Fig. 9   Ohmic heating contours, W/m³, for the NASA Lewis Research Center's arcjet; simulated hydrazine, CNE simulation, $I = 10$ A, $\dot{m} \approx 50$ mg/s (case 2 of Table 1).**
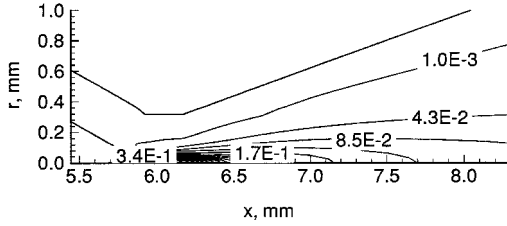
Fig. 10 Ionization fraction contours for the NASA Lewis Research Center's arcjet; simulated hydrazine, CNE simulation, $I = 10$ A, $\dot{m} \approx 50$ mg/s (case 2 of Table 1).

electric heating of the plasma. The peak ohmic heating just off the cathode tip is $j^2/\sigma \approx 3.6 \times 10^{13}$ W/m^3 (not shown in Fig. 9). The heating is largely confined to the central region of the flow, as indicated by high radial gradients in j^2/σ. Strong radial electric fields produce elevated heating near the anode, $\sim 10^{10}$ W/m^3. The j^2/σ distribution is qualitatively similar to the electron temperature. The high near-anode heating couples with low electron populations to produce the high degree of thermal nonequilibrium.

Figure 10 illustrates α contours. The plasma near the cathode tip is highly ionized, with $\alpha \geq 0.6$. In the constrictor region, levels of $\alpha \geq 0.01$ are maintained over roughly 50% of the nozzle radius. The distribution of σ is largely determined by the ionization fraction and the electron temperature. In the hot, highly ionized arc region, $\sigma \approx 5000-10,000$ (Ω-m)$^{-1}$, corresponding to the Spitzer limit, where σ is controlled by large cross section electron–ion coulomb collisions. The σ decreases with radius, eventually reaching ≈ 0.7 (Ω-m)$^{-1}$ at the current attachment region of the anode. The flow is molecule-rich in this region. The plasma conductivity near the anode is primarily determined by the elevated electron temperature, the electron–molecule collision cross sections, and the finite, non-zero ionization levels of $\alpha \approx 10^{-4}$.

Generalized Ohm's Law

The preceding results are obtained with the electron pressure gradient term neglected in generalized Ohm's law. There were concerns that the electron gradient term might significantly affect the current distribution in the arcjet. Moreover, there are uncertainties in the value of δ. Hence, the sensitivities of the MKB model results to the electron pressure gradient term and δ were investigated.

The correct approach to the arc attachment problem is to model the anode as an equipotential surface, and to allow the current distribution to be a model output that is independent of artificial restrictions. This self-consistent approach solves the current distribution and electric field simultaneously, for which the current distribution is properly coupled to the flowfield. The Ohm's law expression for current density in partially ionized gases can be written in generalized form as[12]

$$j = \sigma \left\{ E + \frac{\nabla p_e}{en_e} - \frac{j \times B}{en_e} - \frac{f^2 \tau_{ln}}{m_l n_e}[(2 - \alpha)p_e \times B + B \right.$$
$$\left. \times (j \times B)] \right\} \qquad (2)$$

$$\nabla \cdot j = 0 \qquad (3)$$

where the first term accounts for the electric field, the second term accounts for electron pressure gradients, the third term is the Hall effect, and the last term is ion current. Because the plasma is electrically neutral and $B \approx 0$, then $E = -\nabla V$ and the last two terms may be neglected. In Refs. 1, 4, and 8, the electron pressure gradient term is also neglected, and the expression for current density is
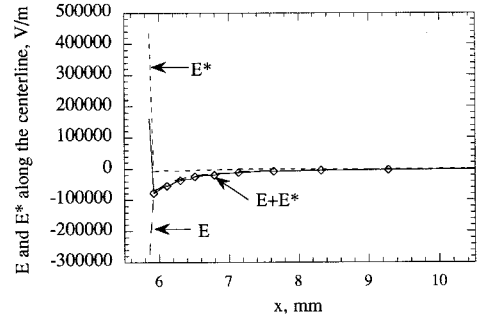
$$j = -\sigma \nabla V \qquad (4)$$

Fig. 11 Electric fields E and E^* induced by electron pressure gradient along the centerline with $\delta_{N_2} = \delta_{H_2} = 3000$ and Eq. (5). Note that the constrictor is 0.25 mm long, and is located between $x = 5.92$ and 6.17 mm.

Here we present results using Eq. (2) to include the electron pressure term. Thus,

$$j = \sigma[-\nabla V + (\nabla p_e/en_e)] = \sigma(E + E^*) \qquad (5)$$

where

$$E^* \equiv \nabla p_e/en_e \qquad (6)$$

Numerical instabilities can be encountered in the incorporation of the electron pressure gradient term, caused by the enormous electron pressure gradient in the cathode tip region. To obtain a stable solution, the electron pressure term has to be rewritten in the form

$$\frac{\nabla p_e}{en_e} = \frac{\nabla(n_e k_b T_e)}{en_e} = \frac{k_b T_e}{e} \nabla \ln n_e + \frac{k_b}{e} \nabla T_e \qquad (7)$$

Note that the gradient of $\ln(n_e)$ is much less severe than that of p_e. This stabilized the code.

The axial electric fields E and E^* are shown in Fig. 11. E^*, induced by the electron pressure gradient, is very strong at the cathode tip, and has the opposite sign of E. E^* rapidly decreases to less than E in magnitude one node into the constrictor, at $x \approx 6$ mm. Downstream of $x \approx 6$ mm, both E and E^* are small.

The predicted electron number density distribution (as well as the electron and heavy-species temperature distributions) changes only slightly when Eq. (5), instead of Eq. (4), is used. The predicted plasma voltage decreases from 74 to 71 V when the electron pressure gradient is included in Ohm's law. Overall, the electron pressure gradient term did not significantly affect the current distribution, and could be neglected if approximate results were desired.

Inelastic Electron–Molecule Collisions

The assumption of thermal nonequilibrium requires independent energy equations for the electrons and extra heavy species (molecules, atoms, and ions). In the MKB model, the electron energy is separated from the total energy, allowing for a distinct T_e. The electron kinetic energy is negligible, so that energy conservation is written as

$$\nabla \cdot \left[C_{pe} T_e \left(n_e v - \frac{j}{e} \right) \right] = \nabla \cdot (\lambda_e \nabla T_e)$$
$$+ \nabla \cdot \left(\frac{1}{m_e} \rho C_{pe} T_e D_e \nabla y_e \right) + \frac{j \cdot j}{\sigma} - elst$$
$$- \text{radiation} - \sum L_e \qquad (8)$$

Here, $j = \sigma(E + E^*)$ is assumed to be primarily electron current, so that the convection of the electrons caused by the mean

flow velocity v is reduced by the drift flux of electrons j/e. The convection of electron energy is balanced by thermal conduction, energy transport as a result of diffusion, and ohmic heating. Additionally, the electrons lose energy through elastic and inelastic collisions with molecules, atoms, and ions[13] and through optically thin radiation loss caused by continuum bremsstrahlung.[14] The energy loss caused by elastic transfer is

$$elst = 3k_b(T_e - T_g)n_e m_e \sum_{i \neq e} \frac{\bar{\nu}_{ei}}{m_i} \qquad (9)$$

where $\bar{\nu}_{ei}$ are calculated using the mean electron thermal speed, n_i, and Q_{ei}, as[14]

$$\bar{\nu}_{ei} = \sqrt{(8k_b T_e/\pi m_e)}n_i Q_{ei} \qquad (10)$$

In this research, the ionization and recombination processes for H and N are included in the finite rate chemistry model; thus, these inelastic losses are accounted for in the ΣL_e term in Eq. (8). To account for electron energy losses to molecular vibration, rotation, electronic excitation, and ionization modes during the electron–molecule inelastic collision, the electron energy loss during the collision is modeled as δ times the elastic loss:

electron energy loss during an electron–molecule

$$\text{inelastic collision} = elst + \sum_i L_e \equiv \delta_i \cdot elst \qquad (11)$$

where the expression for $elst$ is given in Eq. (9), and the subscript i denotes either H_2 or N_2. This is necessary because the molecular excited states are not treated as separate species in the finite rate chemistry model. Although δ_{H_2} and δ_{N_2} are generally energy dependent, $\delta_{H_2} = \delta_{N_2} = 3000$ was chosen for the majority of the simulations in Refs. 1, 4, and 8. Note that Martinez-Sanchez and Miller[15] re-examined δ_{N_2}, and found values as high as $\delta_{N_2} = 4000$.

Parametric studies[8] showed that the current attached to the constrictor region and the predicted plasma voltage drop was only 40 V at 10 A when δ, from Ref. 12, on the order of 10–100, was used. Increasing δ moved the arc attachment location downstream of the constrictor, in agreement with measurements of the current distribution using segmented anodes[16] and anode probe measurements.[6] The values of $\delta_{N_2} = \delta_{H_2} = 3000$ were chosen for the majority of the simulations because reasonable convective effects were noted, as the arc was swept farther downstream for increasing mass flow rate, and better agreement was achieved between the predicted and experimentally observed operating voltage of 115 V for the hydrazine CNE simulation (cases 2 and 10, Table 1).

The motivation for the present analysis stems from the potential uncertainties in δ. These are summarized in Fig. 12, where the loss factors from various sources are plotted as a
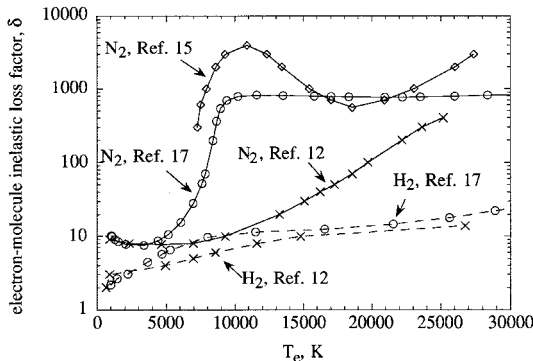

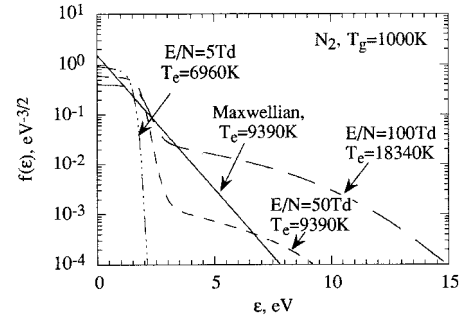Fig. 12 δ from various sources.

Fig. 13 Calculated f for various ratios of E/N for a nitrogen plasma.[17] The Maxwellian distribution function is a straight line.

function of T_e. A software package, MacELENDIF (Ref. 17), is also used to estimate δ_{N_2} and δ_{H_2}.

The ELENDIF software solves the time-dependent Boltzmann transport equation.[18] The software was used to calculate $f(\varepsilon)$ for weakly ionized hydrogen or nitrogen plasmas. The δ factor was extracted from the relative percentages of inelastic and elastic energy losses using the relation

$$\delta = 100/\% \text{ of elastic energy transfer} \qquad (12)$$

The effective electron temperature was calculated from the mean electron energy. This was necessary because the distributions can be non-Maxwellian.

The δ factor is dependent strongly on the collision partner and the electron temperature, and weakly on the gas temperature. Moreover, in a 1-kW arcjet, the molecule-rich anode region is slightly above the wall temperature, and so the gas (molecule) temperature was chosen to be 1000 K for both hydrogen and nitrogen simulations. The δ_{H_2} values were fitted by a sixth-order polynomial, and the δ_{N_2} values by four piecewise polynomials, to incorporate δ into the MKB model.

Figure 12 shows δ_{N_2} and δ_{H_2} calculated by ELENDIF, with δ_{N_2} from Refs. 12 and 15 and δ_{H_2} from Ref. 12. The ELENDIF results indicate $\delta_{N_2} \approx 800$ for T_e above 10,000 K, while the δ_{H_2} are in rough agreement with those from Ref. 12. The results from Ref. 15 indicate a maximum $\delta_{N_2} \approx 4000$ at $T_e \approx 10,000$ K. The δ_{N_2} from Ref. 15 are mostly higher than the results of ELENDIF. Thus, it appears that when $T_e > 10,000$ K, the appropriate values for δ_{H_2} and δ_{N_2} may be of order 10 and 800, respectively. The discrepancies among the δ_{N_2} values require further investigation.

The implications of the high degree of inelastic losses may be further appreciated by examining representative calculations for the electron energy distribution functions.[17] Results for N_2 are shown in Fig. 13 for three ratios of E to N. For respective values of $E/N = 5$, 50, and 100 Td [1 townsend (Td) = 1 $\times$ 10^{-17} V-cm^2], the effective temperatures are $T_e = 2\varepsilon_{av}/3k_b \approx$ 6960, 9390, and 18,340 K, respectively. (Note that $E/N \approx 65$ Td for typical near-anode predictions of $E \approx 250$ V/mm, $p \approx$ 1 atm, and $T_g \approx 1000$ K.) The Maxwellian-distribution function

$$f(\varepsilon) = \frac{2}{\sqrt{\pi}(k_b T_e)^{3/2}} \exp\left(\frac{-\varepsilon}{k_b T_e}\right) \qquad (13)$$

appears as a straight line with a slope inversely proportional to T_e in Fig. 13. The distributions are clearly non-Maxwellian. The inelastic losses into the vibration and rotation modes of N_2 reduce significantly the number of electrons at the higher translation energies, and lead to an overpopulation at the lower energies. Because, as appears likely, distributions similar to those indicated in Fig. 13 occur in the arcjet plasma, then the electron-impact ionization and dissociation chemical rate coefficients used in the present model may incur substantial errors. The cross sections and the rate coefficients are energy-
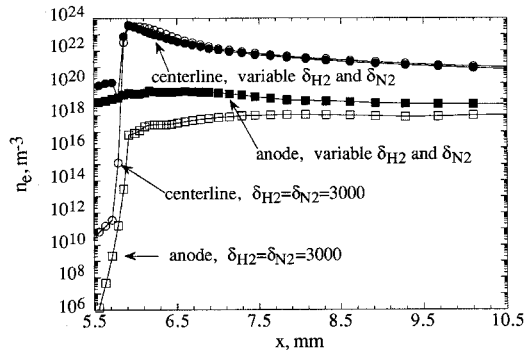
Fig. 14 Electron number density at the centerline and the anode for $\delta_{N_2} = \delta_{H_2} = 3000$ and variable δ_{N_2} and δ_{H_2} from Ref. 17.
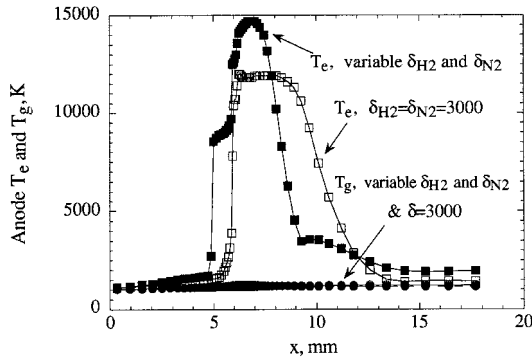

Fig. 15 Electron and heavy-species temperature along the anode for $\delta_{N_2} = \delta_{H_2} = 3000$ and variable δ_{N_2} and δ_{N_2} from Ref. 17.

averaged over a Maxwellian-distribution function, and thus will introduce similar errors in the electrical conductivity.

Figure 14 indicates that the electron number density along the centerline is similar for both the variable δ and $\delta_{H_2} = \delta_{N_2} = 3000$ cases. The electron number density at the anode wall is much higher for the variable δ case compared with the $\delta_{H_2} = \delta_{N_2} = 3000$ case, causing the plasma voltage to drop from 71 V ($\delta_{H_2} = \delta_{N_2} = 3000$) to 50 V (variable δ).

When assuming an artificially larger $\delta_{H_2} = \delta_{N_2} = 3000$, the energy transfer from the electrons to the heavy species is increased. Hence, the thermal diffusivity of the electrons is lowered. This low thermal diffusivity enables the electrons to flow downstream rather than to diffuse radially to the anode. When the variable (smaller) δ factors from ELENDIF are used, the thermal diffusivity of the electrons increases. This results in an increased anode electron temperature upstream (Fig. 15). As a result, the electrons diffuse to the anode wall in a more upstream location, and this, coupled with higher σ, causes the plasma voltage to decrease by 21 V.

Additional effects of the electron–molecule inelastic loss δ factor are investigated by comparing the predictions summarized as cases 3, 4, and 5 in Table 1. For the NASA Lewis Research Center's arcjet geometry, I is constant at 10 A, while the mass flow rate is approximately 50 mg/s. Simulations were performed using $\delta_{H_2} = \delta_{N_2} = 3000$, 300, and 30. The results indicate that the anode attachment location, and hence the total voltage, are strongly dependent on the δ factor. With $\delta_{H_2} \approx 10$ and δ_{N_2} increased from 800 to 4000, the total arcjet voltage increases from 88 to 101 V (cases 6, 7, and 8 in Table 1), which is still 14 V lower than the experimentally observed[7] 115 V. Hence, uncertainties in δ_{N_2} do not produce a large variation in voltage as long as $\delta_{H_2} \approx 10$.

The results in Table 1 indicate that increasing x_{cat} increases the total voltage (cases 2, 3, and 4). The reason is that increasing the cathode gap increases the length of the arc, and this causes the plasma resistance to increase. The total voltage then increases to maintain the same current (current = total

voltage/plasma resistance). The predicted total voltage and specific impulse from the CNE simulation with $\delta_{H_2} = \delta_{N_2} = 3000$ (cases 2 and 9 in Table 1) are within $\pm5\%$ of the experimental measurements (case 10). The predicted efficiencies (cases 2 and 9) are 5–6% higher than the experimental value (case 10).

Conclusions

A detailed nonequilibrium 1-kW hydrazine arcjet model (the MKB model) has been used successfully to interpret the complicated physics of the arcjet. The model treats thermal and chemical nonequilibrium, which includes finite rate chemical kinetics and mass diffusion. The model is geometry-flexible, and also includes a thermal model for the anode. These features make the description sufficiently comprehensive for continuing arcjet analyses and design studies. The MKB model is currently the only 1-kW hydrazine arcjet model that treats two-dimensional flow and thermal and chemical nonequilibrium.

Major conclusions are summarized as follows:

1) A nonequilibrium description of the plasma flowfield is required to model arcjet physics accurately. The thermal nonequilibrium CNE model reveals a high degree of thermal nonequilibrium near the electrode surfaces. The predicted thermal nonequilibrium near the anode is $T_e/T_g \approx 12$, and is in qualitative agreement with the $T_e/T_g \approx 10$–20 from anode probe measurements.[6] The large thermal nonequilibrium is responsible for increased ionization rates. The elevated population of charged species permits the conduction of electric current through near-anode regions of the plasma, where T_g is low. The incorporation of a separate energy equation for the electron gas is required to capture this arc conduction mechanism.

The CNE simulations reveal radial ambipolar diffusion as a significant factor. The radial diffusion of charged species also controls the near-anode electron populations. The chemical nonequilibrium predictions indicate a reduced arc length, partially from radial ambipolar diffusion. The incorporation of finite rate chemistry also permits a more accurate description of the inelastic energy exchange between the electrons and heavy species.

2) Finite rate chemistry models are required to accurately capture the flowfield species distributions. Radial species diffusion is also important. The dissociated H and N atoms diffuse from the hotter central region of the flow to the cooler anode wall. Diffusive transport of the molecular N_2 and H_2 species from the cooler anode radially inward to the hot central flow region is also significant.

3) The anode arc attachment is strongly dependent on the chosen value for the electron–molecule inelastic collision factor δ. Generally, the arc attaches farther downstream and the plasma voltage increases as δ increases. Large variations in δ_{H_2} and δ_{N_2} (from 300 to 3000) produce a 7-V change in the arcjet voltage, similar to that caused by a 76% increase in cathode gap (cases 2, 3, and 4 in Table 1).

4) The predicted global performance and local variables generally follow experimental measurements. The predicted total V and I_{sp} for hydrazine is within $\pm5\%$ of measured values (cases 2, 9, and 10 in Table 1). The slight underpredictions in V and overpredictions in I_{sp} translate to overpredictions in η of 5–6% over the experimental value (cases 2, 9, and 10).

Correctly predicting arc attachment location and operating voltage is of paramount concern for continuing research. As the arcjet community moves to higher specific power designs, the anode current density distribution will ultimately determine the severity of the anode thermal loading, and therefore the long-term reliability of the thruster.

Acknowledgments

References

[1]Megli, T. W., Krier, H., and Burton, R. L., "Plasmadynamics Model for Nonequilibrium Processes in N$_2$/H$_2$ Arcjets," *Journal of Thermophysics and Heat Transfer*, Vol. 10, No. 4, 1996, pp. 554–562.

[2]Miller, S. A., and Martinez-Sanchez, M., "Two-Fluid Nonequilibrium Simulation of Hydrogen Arcjet Thrusters," *Journal of Propulsion and Power*, Vol. 12, No. 1, 1996, pp. 112–119.

[3]Fujita, K., "Performance Computation of a Low-Power Hydrogen Arcjet," AIAA Paper 96-3183, July 1996.

[4]Megli, T. W., Krier, H., Burton, R. L., and Mertogul, A., "Two-Temperature Modeling of Nitrogen/Hydrogen Arcjets," *Journal of Propulsion and Power*, Vol. 12, No. 6, 1996, pp. 1062–1069.

[5]Lu, J., Krier, H., Burton, R. L., and Goodfellow, K. D., "Collisionless Cathode Sheath Models to Predict Power Distribution in 1 kW Hydrazine Arcjet Thrusters," AIAA Paper 97-3206, July 1997; also *Journal of Thermophysics and Heat Transfer* (submitted for publication).

[6]Tiliakos, N. T., Burton, R. L., and Krier, H., "Arcjet Anode Plasma Measurements Using Electrostatic Probes," AIAA Paper 97-3201, July 1997; also *Journal of Propulsion and Power* (to be published).

[7]Curran, F. M., and Haag, T. W., "Extended Life and Performance Test of a Low-Power Arcjet," *Journal of Spacecraft and Rockets*, Vol. 29, No. 4, 1992, pp. 444–452.

[8]Megli, T. W., "A Nonequilibrium Plasmadynamics Model for Nitrogen/Hydrogen Arcjets," Ph.D. Dissertation, Dept. of Mechanical and Industrial Engineering, Univ. of Illinois, Urbana, IL, 1995.

[9]Bose, T. K., "Thermophysical and Transport Properties of Multi-Component Gas Plasmas at Multiple Temperatures," *Progress in Aerospace Sciences*, Vol. 25, No. 1, 1988, pp. 1–42.

[10]Richley, E., and Tuma D. T., "On the Determination of Particle Concentrations in Multitemperature Plasmas," *Journal of Applied Physics*, Vol. 53, No. 12, 1982, pp. 8537–8542.

[11]Zube, D. M., and Myers, R. M., "Thermal Nonequilibrium in a Low-Power Arcjet Nozzle," *Journal of Propulsion and Power*, Vol. 9, No. 4, 1993, pp. 545–552.

[12]Sutton, G. W., and Sherman, A., *Engineering Magneto-Hydrodynamics*, McGraw–Hill, New York, 1965, pp. 148–190.

[13]Kruger, C. H., and Mitchner, M., "Kinetic Theory of Two Temperature Plasmas," *Physics of Fluids*, Vol. 10, No. 9, 1967, pp. 1953–1961.

[14]Mertogul, A. E., "Modeling and Experimental Measurements of Laser Sustained Plasmas," Ph.D. Dissertation, Dept. of Mechanical and Industrial Engineering, Univ. of Illinois, Urbana, IL, 1993.

[15]Martinez-Sanchez, M., and Miller, S. A., "Arcjet Modeling: Status and Prospects," *Journal of Propulsion and Power*, Vol. 12, No. 6, 1996, pp. 1035–1043.

[16]Curran, F. M., Manzella, D. H., and Pencil, E. J., "Performance Characterization of a Segmented Anode Arcjet Thruster," AIAA Paper 90-2582, June 1990.

[17]Morgan, W. L., and Penetrante, B. M., MacELENDIF version 1.1, Kinema Software, 1994.

[18]Morgan, W. L., and Penetrante, B. M., "ELENDIF: A Time-Dependent Boltzmann Solver for Partially Ionized Plasmas," *Computer Physics Communications*, Vol. 58, Nos. 1 and 2, 1990, pp. 127–152.